

See discussions, stats, and author profiles for this publication at: <https://www.researchgate.net/publication/235435036>

Design and In Vivo Evaluation of a Robotized Needle Insertion System for Small Animals

Article in IEEE transactions on bio-medical engineering · August 2013

DOI: 10.1109/TBME.2013.2243728

CITATIONS

9

READS

317

7 authors, including:



Laurent Goffin

IHU - Institut de chirurgie guidée par l'image

27 PUBLICATIONS 199 CITATIONS

[SEE PROFILE](#)



Fernand Martel

2 PUBLICATIONS 20 CITATIONS

[SEE PROFILE](#)



Gaétan Bour

Merck Millipore

24 PUBLICATIONS 721 CITATIONS

[SEE PROFILE](#)



Stéphane André Nicolau

european patent office, Munich, Germany

95 PUBLICATIONS 2,057 CITATIONS

[SEE PROFILE](#)

Some of the authors of this publication are also working on these related projects:



teensySHOT [View project](#)



Educational publications [View project](#)

Design and *In Vivo* Evaluation of a Robotized Needle Insertion System for Small Animals

Laurent Goffin, Gaétan Bour, Fernand Martel, Stéphane Nicolau, Jacques Gangloff, Jean-Marc Egly, and Bernard Bayle*

Abstract—The development of imaging devices adapted to small animals has opened the way to image-guided procedures in biomedical research. In this paper, we focus on automated procedures to study the effects of the recurrent administration of substances to the same animal over time. A dedicated system and the associated workflow have been designed to percutaneously position a needle into the abdominal organs of mice. Every step of the procedure has been automated: the camera calibration, the needle access planning, the robotized needle positioning, and the respiratory-gated needle insertion. Specific devices have been developed for the registration, the animal binding under anesthesia, and the skin puncture. Among the presented results, the system accuracy is particularly emphasized, both *in vitro* using gelose phantoms and *in vivo* by injecting substances into various abdominal organs. The study shows that robotic assistance could be routinely used in biomedical research laboratories to improve existing procedures, allowing automated accurate treatments and limited animal sacrifices.

Index Terms—Medical robotics, robotized needle insertion, small animal.

I. INTRODUCTION

RODENTS are frequently used as models for human diseases, both for testing new therapeutic drugs and understanding disease evolution. Drug testing requires the administration of substances into an organ or a structure such as a tumor. The pathology evolution is then ideally investigated from biopsies, to prevent animal sacrifice. Both procedures require accurate and repeatable percutaneous needle positioning, which can be improved by image-guided robotic assistance. Needle insertion robotic systems have already been proposed for small animals, using either commercial or custom-made robotic manipulators, guided by various imaging modalities. To compare

Manuscript received August 1, 2012; revised December 3, 2012; accepted January 13, 2013. Date of publication March 7, 2013; date of current version July 13, 2013. This work was supported by Region d'Alsace, ARC and ANR. *Asterisk indicates corresponding author.*

L. Goffin and J. Gangloff are with the ICube Laboratory, UMR CNRS 7357, University of Strasbourg, Strasbourg 67400, France (e-mail: lgoffin@unistra.fr; jacques.gangloff@unistra.fr).

G. Bour and S. Nicolau are with the Institut de Recherche contre le Cancer de l'Appareil Digestif, Strasbourg 67000, France (e-mail: gaetan.bour@ircad.fr; stephane.nicolau@ircad.fr).

F. Martel and J.-M. Egly are with the Institut de Génétique et de Biologie Moléculaire et Cellulaire and the Institut de Recherche contre le Cancer de l'Appareil Digestif, Strasbourg 67000, France (e-mail: fernand.martel@ircad.fr; jean-marc.egly@igbmc.fr).

*B. Bayle is with the ICube Laboratory, UMR CNRS 7357, University of Strasbourg, Strasbourg 67400, France (e-mail: bernard.bayle@unistra.fr).

Color versions of one or more of the figures in this paper are available online at <http://ieeexplore.ieee.org>.

Digital Object Identifier 10.1109/TBME.2013.2243728

existing studies, the needle tip position accuracy and the experimental conditions are of particular interest.

Kazandides *et al.* [1] proposed a μ PET-guided system to measure the tissue oxygen tension level in tumors cells. It allows inserting into rodent tumors an oxyLite probe through a cannula using a dedicated 3 degrees of freedom (DOF) robotic arm [2]. The arm is composed of a Cartesian horizontal platform and two vertical slides, one for the cannula and one for the probe. Four fiducials on the rodent bed are used to register the bed position in the robot frame. The estimated mean positioning error is 0.4 mm in phantom tests. Huang *et al.* [3] proposed a system based on a 5 DOF robotic arm with three translations and two rotations, called the CAST-PRO II. After a MR- μ PET image fusion, the accuracy of the robotic system is about 0.05 mm and the mean positioning error in a phantom is 1.2 mm. Waspe *et al.* [4] designed a 6 DOF robotic system with a remote center of motion (RCM). Its was coupled with ultrasound imaging in [5] and later with μ CT imaging in [6]. This system is designed so as to be placed near the imaging zone, since it is quite small and compact. As every system using an RCM, the entry point must be very precisely placed, which is the case in the presented results: Waspe *et al.* exhibit the best accuracy results among the relevant publications in the field, with an accuracy of 0.1–0.15 mm for both imaging modalities. In these works, the performances were evaluated with euthanized animals.

Bebek *et al.* [7] designed a compact parallel 5 DOF robot, composed of a front stage with 2 DOF and a back stage with 3 DOF. The accuracy of the robot is estimated by following a line with a pencil on a white paper. The pencil tip thickness is 0.5 mm and the mean position error is around 2 mm [8]. More recently, the same authors could decrease this positioning error to 0.4 mm using an adequate calibration procedure [9]. Ramrath *et al.* [10] designed a needle positioning robot with 5 DOF, the SASSU system, dedicated to stereotactic neurosurgery in the small animal. The very good accuracy results (mean positioning error of 0.03 mm) presented in [10] characterize the robotic system itself, since they have been obtained in the free space, without medical imaging registration, as for Bebek *et al.* previously. Such evaluations are then not strictly comparable to the previous ones, for which an imaging device has been used.

Table I sums up the different systems characteristics and the experimental conditions used in the evaluation (in the chronological order). The obtained results have to be compared taking into account these experimental conditions. In particular, it is interesting to note that, to the best of our knowledge, none of these publications report *in vivo* results, though it is a perspective claimed in several papers.

TABLE I
PREVIOUS WORKS: EXPERIMENTAL CONDITIONS AND RESULTS

| Authors | DOF | Imaging dev. | Validation | Accuracy |
|----------------|-----|--------------|------------|----------|
| Kazandides [1] | 3 | MicroPET | PH | 0.4 mm |
| Huang [3] | 5 | MR and PET | PH | 1.2 mm |
| Waspe [11] | 6 | Ultrasonic | EM | 0.1 mm |
| Ramrath [10] | 5 | None | LAB | 0.03 mm |
| Waspe [6] | 6 | CT | EM | 0.15 mm |
| Bebek [9] | 5 | None | LAB | 0.4 mm |

PH = Phantom, EM = Euthanized mouse, LAB = Laboratory experiments.

In this paper, we focus on automated procedures for percutaneous needle insertions in small animals, in order to be able to correctly assess the effects of recurrent administration of substances to the same animal over time. The aim of the presented system is to save time to the operator by automating many procedure steps, while obtaining good accuracy performances, in the difficult context of percutaneous needle insertions in soft tissues, in the small animal. This system and its workflow have been purposely designed and evaluated. The system is composed of a μ CT-scanner, an instrumented mouse bed, a robotic system, and a stereo camera. It allows performing automated injections and biopsies. The system design and its evaluation, particularly using *in vivo* experiments are the main contributions of this paper. This paper notably extends the preliminary results published in [12], in particular, by providing *in vivo* evaluation.

This paper is organized as follows. The proposed approach and the designed system are presented in Section II. Preoperative calibration methods used to compute the stereo camera parameters and the cameras/robot transformation are presented in Section III. Then, the registration issue is developed in Section IV. The technique used to obtain accurate needle positioning by visual servoing is presented in Section V. Section VI details the experimental evaluation of the whole system, with both phantom and *in vivo* tests. Finally, conclusions and perspectives are given.

II. SYSTEM DESIGN

A. Biological Constraints

The design of a robotized solution for percutaneous needle insertion in rodents requires to take into account some specific constraints that have been identified.

- 1) *Anesthesia*: For animal immobilization and to reduce pain, mice are anesthetized with Isoflurane, always less than 1 h.
- 2) *Asepsis*: Skin and needle must be sterile.
- 3) *Breathing*: The image acquisition and the puncture have to be synchronized with the breathing cycles to take into account the organs motions.
- 4) *Percutaneous insertion*: The skin of mice being very elastic, the needle insertion cannot be performed without compressing the abdomen.

B. Setup

To our knowledge, there is no commercial interventional μ CT-scanner that may allow performing the needle insertion

within the scanner gantry or even in its neighborhood, in order not to move the animal between image acquisition and needle insertion. While it can be considered as nearly impossible to operate within the gantry (typically 13–20 cm internal diameter), an elegant solution would be to place the robotic insertion system at the extremity of the animal bed, outside the scanner, to perform the insertion after an horizontal slow translation of the animal in its bed. It is the solution implemented in [6], but in spite of the robot placement near the imaging zone, the insertion procedure requires an extra motion to place conveniently the animal for needle insertion. We also studied such a solution, but it was finally considered too much scanner dependent and not versatile enough. Actually, it can be pointed out that the scanner configuration may allow (or not) placing the robot in the neighborhood of the animal bed. Some scanners, such the one used in the following, are protected by an unremovable door that prevents easy access to the animal bed, for radio-protection concerns.

Another important consideration in the setup design was to provide flexibility, so as to allow its use with different needle insertion procedures, with a special interest for insertions in soft tissues. The system should use injection or biopsy needles, with different shapes and lengths. As no needle manufacturing process can guarantee a perfect and systematic reproduction of the needle geometric parameters, the procedure and setup have to perform well even in the presence of disparities in the geometry of the needle, and in its mounting on the robot. This is the reason why we proposed to position and rotate the needle tip using a closed-loop strategy based on external camera measurements.

Finally, the proposed approach relies on a dedicated robotic cell, in which the mouse bed is placed after image acquisition. The robotic cell is designed both to position and register the animal efficiently, and to perform accurate needle insertions. The robotic arm used to position the needle is computer vision guided, in order to reach the target specified in the tomographic images with a high accuracy. For the registration of the needle trajectory and for the robot guidance, the cell is equipped with a stereo vision system. With this system and the appropriate procedures, we expect to reach a positioning accuracy below 1 mm, compatible with the size of the visible tumors in mouse liver (image resolution: 0.12 mm).

The setup is presented in Fig. 1. It includes: i) the μ CT-scanner used to acquire images in which the needle path is planned; ii) the robotic arm with its dedicated needle holder; iii) the bed designed to limit animal motions and to perform the registration; iv) the stereo camera system used for registration and visual servoing. These different elements will be detailed in the remainder of the section, but first the procedure workflow is explained.

C. Workflow

The system workflow is presented in Fig. 2. It is composed of manual and automatic steps. The whole procedure lasts an average 35 min (sum of the times in the figure and of some delays between tasks). It includes 15 min of image acquisition that cannot be decreased to preserve the image resolution

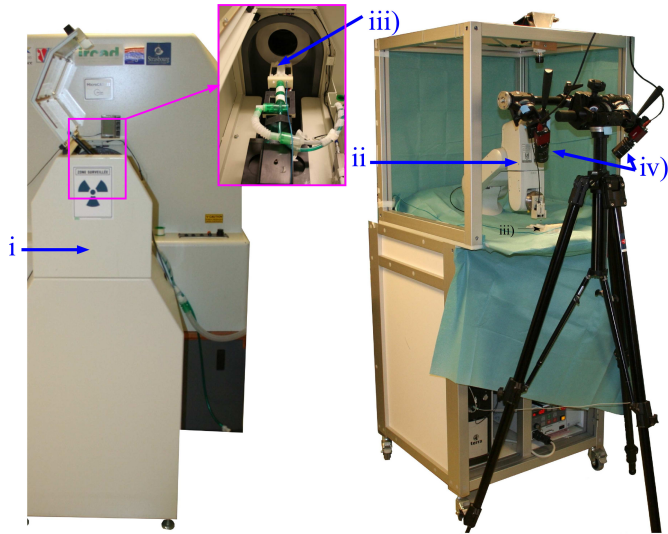


Fig. 1. Imaging and robotic setup.

for the application. Indeed, the voxel size was set to $0.119 \text{ mm} \times 0.119 \text{ mm} \times 0.119 \text{ mm}$, and the acquisitions were respiratory gated on the rest phase of the respiratory cycle. At the rate of 30 respirations per minute, recommended for anesthetized mice, the acquisition lasts 12 min, plus 3 min for volume reconstruction.

After the mouse preparation and positioning in its bed, the image acquisition is performed. The needle insertion is then planned, so as to determine the needle entry point on the animal skin, and the target. The animal is registered using a lid positioned on the top of the bed, which is visible in the μCT -scan images, and also in the video images with structured light (SL) projection. The SL projection is performed once a day, prior to the first experiment, and is used for each μCT scanner/stereocamera registration. After preparing the syringe (for injections), and placing it onto the robot end effector, the needle tip is detected, and it is positioned and rotated using stereo visual servoing. Finally, the animal bed is transferred from the μCT scanner to the robotic cell, the registration lid is removed, and the needle is inserted using a linear actuator.

One of the purpose of the system is to perform fast procedures with limited human interventions. In our workflow, human intervention is required for positioning the mouse on the bed, the bed in the scanner, and finally in the robotic cell. It is also necessary to identify the target and the entry point, and to precisely indicate the registration surface in the computed tomography (CT) images. The operator also launches the different procedures using the human-machine interface (HMI). Note that an adequate graphical user interface has been developed to make the procedure easier for the operator. Finally, he/she pushes the piston to inject the product or make the biopsy. Then, even if the whole procedure is not fully automatic, the operator interventions are limited to the main decisions in the protocol. Besides, these operations do not require advanced knowledge in robotics. Apart from these routines, some calibrations need to be performed from time to time. The stereocamera calibration has not to be performed very often, especially if the cameras are

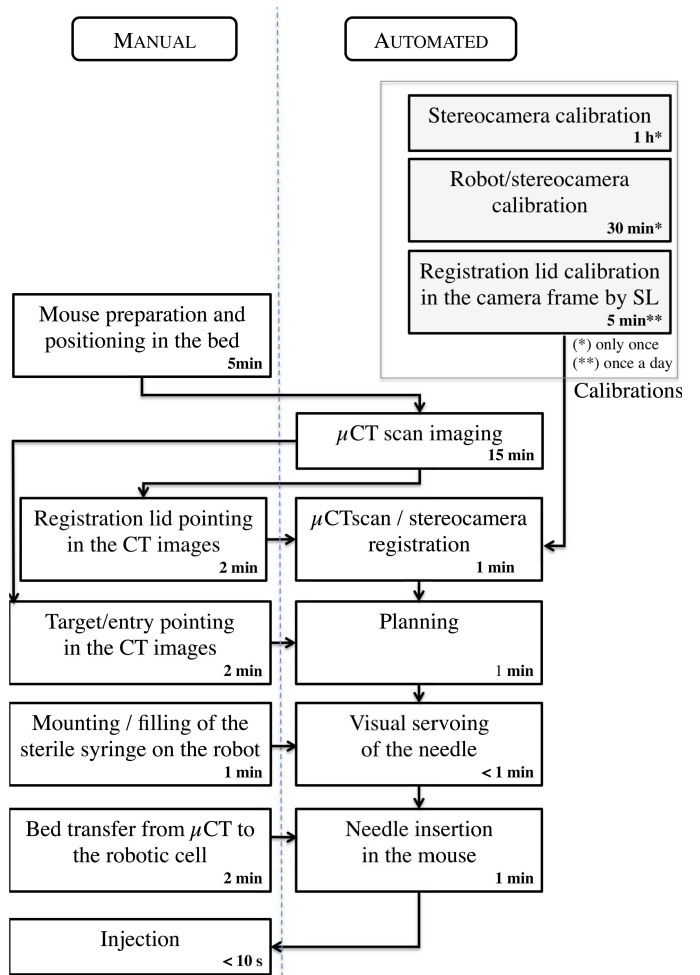


Fig. 2. Procedure workflow (with associated durations).

attached firmly to the robotic cell frame. Finally, the SL registration, which is more frequent, is very simple using the HMI. These calibration procedures will be detailed in the remainder.

D. System Description

1) μCT -Scanner: X-ray CT is used to observe the tumors and plan the needle trajectory. It is also used for the trajectory registration, as the bed is equipped with an adequate surface, easily detected in the images. The micro-CAT II scanner (Imtek, Inc., Siemens) used in this study is dedicated to rodents. With an internal diameter of 13 cm, its gantry is far too narrow for any robotic arm to operate inside the scanner.

The image size of the micro-CAT II is 512^3 voxels with a voxel size of $119 \mu\text{m}$. To minimize the effects of the organs motions, the acquisition is gated on the animal breathing. It is performed between the end of the exhalation and the beginning of the inhalation.

2) Stereo Camera System: A set of two cameras (Allied Vision Technologies Marlin F201B) with an image size of 1600×1200 pixels in 8 bits grey levels is used to accurately locate the needle. For the calibration procedures, a checkerboard is attached to the robot end effector (see Fig. 3). The

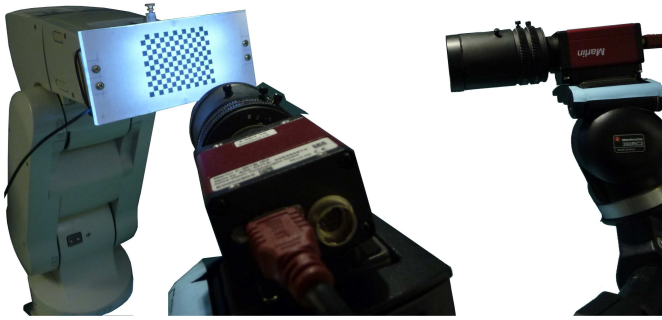


Fig. 3. Stereo camera and a checkerboard attached to the robot.

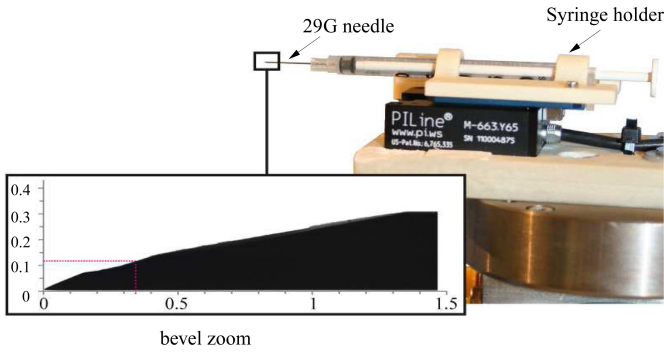


Fig. 4. Percutaneous injector mounted on the robot end effector and micro-CT scan close-up view in mm of the 29G Myjector needle bevel.

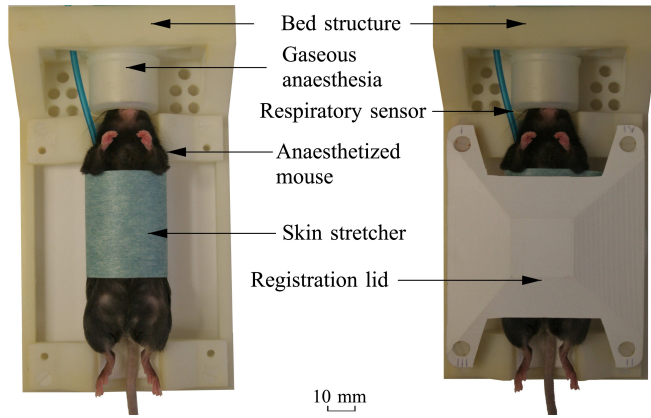


Fig. 5. Mouse bed without (left) and with (right) the registration lid.

checkerboard consists in a grid of $12 \text{ mm} \times 15 \text{ mm}$ black and white $10 \text{ mm} \times 10 \text{ mm}$ squares.

3) *Robotic Cell*: The robotic cell is composed of a 6 DOF Mitsubishi RV1A anthropomorphic arm. The percutaneous injector mounted on the robot end effector (see Fig. 4) includes a specific holder for the syringe translated by a linear motor. A first pneumatic system described in [13] has been replaced by an ultrasonic piezo linear actuator (Physik Instrument M-663.46). This reduces the robot payload and limits the bounce phenomenon at the travel stop. The resulting needle translation is characterized by a 20 mm range, a maximum velocity of 400 mm.s^{-1} , and a resolution of $0.1 \mu\text{m}$.

4) *Mouse Bed and Registration Lid*: The mouse bed (see Fig. 5) has been designed to fit in the μCT -scanner and in the

robotic cell : it has been purposely designed from morphologic data, so that mice are well placed in the bed, and the bed has also been purposely designed so as to adapt to the original scanner bed. Additionally, a system with springs, pushing on two of the bed sides, has been developed to accurately position the bed into the robotic cell, in a repeatable fashion (respectively, $0.07 \pm 0.02 \text{ mm}$ for the positioning repeatability and $0.03 \pm 0.003^\circ$ for the orientation repeatability). The animal is tightly fixed in dorsal decubitus position. A sterile operative field is stuck on the abdomen to stretch the skin and facilitate the puncture. The animal may also be locally shaved to improve the procedure. Since the image acquisition and the needle insertion are gated on breathing cycles, a pressure sensor is integrated to the bed. In addition, the bed is topped with a removable lid, which serves as the registration surface. This lid is placed on the bed during the μCT -scan image acquisition and removed for the insertion phase. The specific shape of the lid has been designed for accurate registration (see details in Section IV-A).

III. CALIBRATIONS

For needle tip positioning, an accurate estimation of the relative pose between the scanner frame and the stereo camera frame is required. This transformation is computed using the bed lid which is visible in both CT and camera views. An SL projection gives a first measurement of the lid surface in the stereo camera frame. This SL reconstruction is then registered with the surface extracted in the CT image. Finally, the planned entry and the target point, defining the needle trajectory, are computed in the stereo camera frame. Since the insertion accuracy relies on the position of these two points, it is mandatory to provide an accurate calibration of the camera set. All the calibrations procedures described in the following have been automated: the checkerboard motions, the corner detection, and the computation of the parameters from the measurements are then automatic. The only manual steps are the mounting of the checkerboard onto the robot end effector and the camera positioning. The HMI enables us to place the cameras very easily in optimal configurations in order to maximize the checkerboard size in the images.

A. Notations

The following notations are used.

- 1) $\{b\}$: robot base frame,
- 2) $\{e\}$: robot end effector frame,
- 3) $\{c_i\}$: i th camera frame,
- 4) $\{sc\}$: common frame of the stereo camera system,
- 5) $\{ch\}$: calibration checkerboard frame,
- 6) $\{n\}$: needle frame (origin = needle tip),
- 7) $\{CT\}$: μCT -scanner frame,
- 8) $\{CAD\}$: CAD (bed and lid design) frame,
- 9) aP : homogeneous coordinates of point P in $\{a\}$,
- 10) aH_b : homogeneous transformation matrix between $\{a\}$ and $\{b\}$, such that ${}^aH_b = {}^aH_c {}^cH_b$ and ${}^aP = {}^aH_b {}^bP$.

B. Calibration of the Stereo Vision System

The calibration consists in determining the intrinsic parameters and the relative pose between both cameras. We propose to calibrate each camera independently in two steps. The relevance of this procedure is discussed at the end of the section.

1) *Calibration of the Intrinsic Camera Parameters*: The calibration of the intrinsic parameters of the cameras is classically performed using Zhang's method [14]. Following the author's notations, the camera model includes the camera focal f_x, f_y , the position of the optical centre in the image c_x, c_y (in pixel), the radial distortion to the second order k_1, k_2 , and the tangential distortion to the second order t_1, t_2 . A checkerboard is used for this calibration, with enough points to ensure a good distortion estimation, since there are four distortion parameters. As suggested by Zhang, the intrinsic parameters are estimated from nine poses with different and symmetrical orientations. In order to reduce the camera sensor noise, ten images are recorded for each checkerboard pose. For each set of ten images, the corner positions are extracted and averaged. The corner detection standard deviation for a static checkerboard position has been estimated around 0.018 pixel.

Let denote $Proj^{c_i} = \{K^{c_i}, k_1^{c_i}, k_2^{c_i}, t_1^{c_i}, t_2^{c_i}\}$ with K^{c_i} the intrinsic parameter matrix and $k_1^{c_i}, k_2^{c_i}, t_1^{c_i}, t_2^{c_i}$ the distortion coefficients of the i th camera.

The criterion minimized for the calibration corresponds to the sum of the squares of the reprojection errors. For a given corner, the reprojection error is the distance between the j th corner extracted in the k th video image $\tilde{m}_{j,k}^{c_i}$ and the 2-D reprojection $m_{j,k}^{c_i}$ of the checkerboard points whose 3-D coordinates are known in $\{ch\}$. Then, the square of the reprojection errors RMS is defined by

$$\min_{Proj^{c_i}} \sum_{j=1}^N \sum_{k=1}^M \left\| \tilde{m}_{j,k}^{c_i} - m_{j,k}^{c_i}(Proj^{c_i}, {}^{c_i}H_{ch,k}) \right\|^2 \quad (1)$$

where M is the number of poses, N the number of corners of the checkerboard, and ${}^{c_i}H_{ch,k}$ corresponds to the pose of the checkerboard frame relative to camera c_i , in image k . The optimization is performed using the Levenberg–Marquardt algorithm and it converges in 62 iterations from an initial reprojection error RMS of 1.04 pixel to a final reprojection error RMS of 0.22 pixel.

This criterion, derived from maximum likelihood theory, is optimal provided that the 2-D points extracted from the video are corrupted by an independent centered Gaussian noise of the same magnitude. In practice, even if it is not perfectly true, this approximation remains relevant.

2) *Calibration of the Camera Relative Poses*: A single image for which the checkerboard is visible by both cameras enables estimating the camera relative poses as ${}^{c_1}H_{c_2} = {}^{c_1}H_{ch} {}^{ch}H_{c_2}$. In this case, the ratio between the number of parameters to be estimated and the number of data is $\frac{6+6}{2N} = \frac{6}{N}$. In order to increase the estimation accuracy, we propose to take more images of the checkerboard in different poses and to minimize the following maximum likelihood criterion, based on the

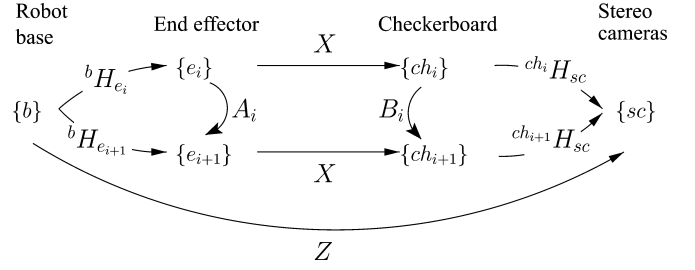


Fig. 6. Frames and transformations in the hand-eye problem.

reprojection error in all the images of both cameras:

$$\min_{\substack{{}^{c_1}H_{ch,k} \\ {}^{c_2}H_{c_1}}} \sum_{j=1}^N \sum_{k=1}^M \left((d_{j,k}^{c_1})^2 + (d_{j,k}^{c_2})^2 \right) \quad (2)$$

where

$$\begin{aligned} d_{j,k}^{c_1} &= \left\| \tilde{m}_{j,k}^{c_1} - m_{j,k}^{c_1}(Proj^{c_1}, {}^{c_1}H_{ch,k}) \right\| \\ d_{j,k}^{c_2} &= \left\| \tilde{m}_{j,k}^{c_2} - m_{j,k}^{c_2}(Proj^{c_2}, {}^{c_2}H_{c_1} {}^{c_1}H_{ch,k}) \right\|. \end{aligned}$$

In this case, the optimization is performed on ${}^{c_1}H_{ch,k}$ and ${}^{c_2}H_{c_1}$, which means a ratio of $6M + 6$ parameters for $2MN$ 2-D point data, i.e., $\frac{3}{N} + \frac{3}{MN} \leq \frac{6}{N}$ as $M \geq 1$. The Levenberg–Marquardt minimization converges from an initial reprojection error RMS of 0.42 pixel to a final reprojection error RMS of 0.19 pixel.

Remark that it is possible to estimate both the intrinsic parameters and the relative camera positions using the data collected in the second step only. To that purpose, the optimization includes the intrinsic parameters in the unknowns, the criterion being the same as previously. However, this approach has two drawbacks. First, it increases the ratio number of unknowns/data, which in turn decreases the optimization stability. Second, it is not compatible with large orientation changes between each pose of the checkerboard. Indeed, the checkerboard rotations have to be limited to keep it visible in both camera views. This means that the distortion estimation will be performed with a set of images in which the checkerboard does not fill the whole images.

In the following, the reference frame of the stereo camera system $\{sc\}$ is arbitrary chosen to be $\{c_1\}$.

C. Robot/Cameras Calibration

As we will see in the following sections, the transformation ${}^bH_{sc}$ between the robot base and the stereo camera has to be known in order to initialize the needle position and to compute the interaction matrix without further experiments.

1) *Hand-Eye or Robot-World Problem Formulation*: The checkerboard mounted on the end effector is detected with the stereo camera system in several poses of the robot. For each pose, ${}^{ch}H_{sc}$ and ${}^bH_{e_i}$ are computed using, respectively, the camera parameters and the robot forward kinematic model. The homogeneous transformation matrices for the i th pose are denoted ${}^{ch_i}H_{sc}$ and ${}^bH_{e_i}$ (see Fig. 6).

Let $A_i = {}^{e_i}H_{e_{i+1}} = {}^{e_i}H_b {}^bH_{e_{i+1}}$ be the relative motion of the end effector and $B_i = {}^{ch_i}H_{ch_{i+1}} = {}^{ch_i}H_{sc} {}^{sc}H_{ch_{i+1}}$ be the relative motion of the checkerboard. Remark that $X = {}^{e_i}H_{ch}$ is a constant, whatever the pose. It can be computed by solving the

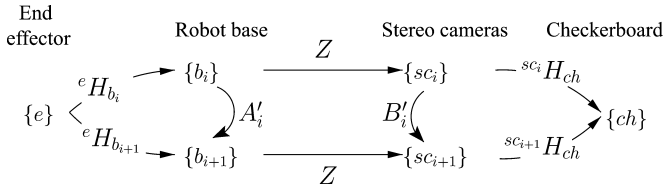


Fig. 7. Frames and transformations in the robot-world problem.

TABLE II
RESIDUAL ERROR MATRICES COMPUTATION

| | | |
|------------|-------------------------------|---|
| X loop | $AX = XB$ | $E_x = B^{-1}X^{-1}AX$ |
| Z loop | $A'Z = ZB'$ | $E_z = B'^{-1}Z^{-1}A'Z$ |
| X & Z loop | ${}^bH_e X = Z {}^{sc}H_{ch}$ | $E_{xz} = {}^{ch}H_{sc} Z^{-1} {}^bH_e X$ |

TABLE III
EVALUATION OF ROBOT/CAMERAS CALIBRATION

| Method | E_{reproj} | E_{xz} | | E_x | | E_z | |
|--------|---------------------|--------------------|--------------------|--------------------|--------------------|--------------------|--------------------|
| | pixels | mm | deg | mm | deg | mm | deg |
| T | 17.44 | 1.59 ± 0.06 | 0.40 ± 0.01 | 0.27 ± 0.04 | 0.19 ± 0.06 | 0.68 ± 0.13 | 0.20 ± 0.06 |
| D | 16.46 | 1.97 ± 0.03 | 0.55 ± 0.01 | 0.26 ± 0.04 | 0.25 ± 0.08 | 0.67 ± 0.12 | 0.21 ± 0.06 |
| RP | 0.30 | 0.69 ± 0.14 | 0.21 ± 0.04 | 0.26 ± 0.04 | 0.23 ± 0.06 | 0.77 ± 0.22 | 0.24 ± 0.06 |

E_{reproj} : reprojection error RMS.

Methods: T = Tsai, D = Dornaika, RP = Tsai + Reprojection minimization.

classical hand-eye problem equation $AX = XB$ [15], where A and B are, respectively, formed by the concatenation of the A_i and B_i terms.

Note that $Z = {}^bH_{sc}$ can be computed in a similar way. Let $A_i' = {}^{b_i}H_{b_{i+1}} = {}^{b_i}H_e {}^eH_{b_{i+1}}$ be the relative motion of the end effector and $B_i' = {}^{sc_i}H_{sc_{i+1}} = {}^{sc_i}H_{ch} {}^{ch}H_{sc_{i+1}}$ be the relative motion of the checkerboard (see Fig. 7). Then, $Z = {}^bH_{sc}$ which is a constant, can be computed by solving $A'Z = ZB'$, with A' and B' , respectively, formed by the concatenation of the A_i' and B_i' terms.

2) *Solutions*: X and Z are obtained according to the methods proposed by Tsai and Lenz [16] and Dornaika and Horaud [17]. The three following residual error matrices E_x , E_z , and E_{xz} (see Table II) are computed for each pose. If the data were perfect, they should be equal to the identity. E_{xz} is computed once X and Z are known. It allows observing the cumulative and crossed effects due to X and Z estimation errors.

The RMS of the reprojection error for all the points of the checkerboard in all the poses, as well as the mean translation and rotation errors, associated with the residual error matrices are given in Table III.

Although Tsai and Dornaika methods give acceptable residual translation and rotation errors, the RMS of the reprojection error remains quite high. It is even visible when representing the superimposition of the video image and of a virtual robot, whose configuration relies on the Z matrix. To limit the reprojection error, we have developed a new method to refine Tsai or Dornaika results, which will then be used as initializations. It consists in minimizing, in a second step, the reprojection error by a nonlinear minimization method. The improvements obtained using this technique are emphasized in the experimental results of Table III, last row. This refinement of the previous

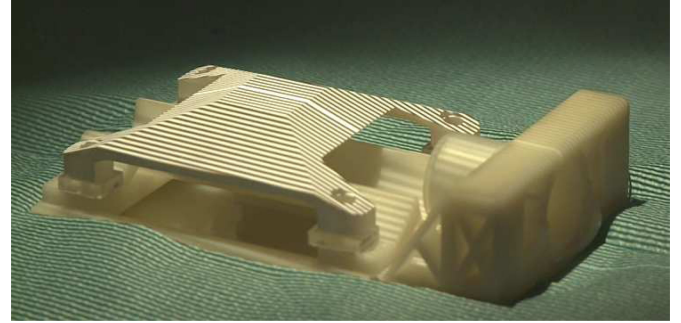


Fig. 8. SL pattern projected on the bed lid.

results is characterized by similar transformation-matrix errors, but it drastically decreases the RMS of the reprojection error. The final error of 0.30 pixel is acceptable for the application.

Remarks: This error has to be compared with the final reprojection error of 0.19 pixel, obtained after the extrinsic calibration. The difference is mainly due to forward kinematic model errors. Experiments consisting in several rotations and translations showed that the first joint of the robot was the source of most positioning error. By blocking this joint during the calibration process, the final error is reduced, as expected. An additional procedure has been implemented to quickly compute the transformation ${}^bH_{sc}$ whenever the cameras are displaced. It uses a tag placed on the robotic cell table, and then rigidly linked to the robot base. When the previously described procedure has been performed once, the tag position is detected in the camera frame, and the camera/tag transformation is computed. The tag is detected in the video images using the ARTAG software library (<http://www.artag.net>). The ARTAG detection is refined by a subpixellic routine implemented with opencv. The tag detection and the transformation computation are quasi-instantaneous and fully automatic.

IV. μ CT-SCANNER/CAMERAS REGISTRATION

This section introduces the methods developed to match points or surfaces of the lid expressed in the CT image with the 3-D reconstruction of a SL pattern projected on the lid.

A. Lid and SL

The lid is a 3-D surface built from five planes with different angles (18° to 25°) with respect to the $22 \times 23 \text{ mm}^2$ horizontal plane on its top. An SL pattern is projected on this surface (see Fig. 8). It is composed of bright and dark stripes. A larger central stripe indicates the pattern origin. The bed and the lid were designed in order to be always placed in the same position in the robotic cell, so that the SL reconstruction is not necessary for each experiment.

Dark lines are detected with a subpixellic resolution [18] in the images of both cameras. Then, they are labeled from the central fringe. Let \tilde{m}^{c_1} be a 2-D point of the i th fringe in c_1 image. The intersection, in the image of camera c_2 , between the epipolar line of \tilde{m}^{c_1} and the i th fringe is computed. It is denoted as \tilde{m}^{c_2} . A 3-D point is then reconstructed from \tilde{m}^{c_1} , \tilde{m}^{c_2} , and

the camera parameters [19]. Finally, a cloud of 10,000 such points of the lid surface, with coordinates expressed in $\{sc\}$, is determined and used for the registration.

B. Registration

Before placing the bed in the robotic cell, the lid registration surface is manually selected, by defining a few points per lid plane in the CT images. Then, the equations of the five planes in $\{CT\}$ are computed by a least square minimization (LSM). These planes can then be registered with the 3-D SL points using a point to plane or a point to point method based on the iterative closest point algorithm [20]. However, a good initialization is required for this classical method, and the obtained accuracy is highly dependent on the points density.

To overcome these two limitations, a plane to plane registration method has been preferred. The five median planes of the lid are computed from the SL points using an LSM with a decimation of 10% of outliers.¹ First, an initial registration is performed with a direct 3-D point to point method [21]. Then, the rotation matrix ${}^{sc}R_{CT}$ is computed by minimizing the sum of the angles between the normals of the lid planes, respectively, known in $\{sc\}$ and $\{CT\}$. As a plane has two opposite normals, the orientation of each plane normal must be the same in both frames, which is obtained by the *a priori* knowledge of the lid geometry. The registration initialization gives an error of 0.45° and the plane to plane registration decreases the error to 0.35° . Finally, the translation ${}^{sc}T_{CT}$ is evaluated by minimization of the distance, for each of the five lid planes, between the point of the plane from $\{sc\}$ and the point of the plane from $\{CT\}$ that are the closest to the origin. A translation error of 0.13 mm is finally obtained.

C. Registration Assessment

The registration errors previously computed are not correlated to the computed transformation accuracy [22]. However, as it could not be directly quantified, we identified indicators of the transformation accuracy.

1) *Projection of SL Points on CT-Scan Planes:* First, the distances between the SL points and the registered lid planes are evaluated by applying the computed transformation. A typical illustration of the registration result is given in Fig. 9. The RMS of the obtained distances is 0.07 ± 0.06 mm, which is less than the μ CT-scan image resolution (0.12 mm).

2) *Projection of the Lid in the Images:* A first qualitative assessment is performed by projecting the lid median planes in the video images. An accurate registration is obtained when the corresponding edges overlap in the images, as shown in Fig. 10.

The projection of the lid model in the μ CT-scan images is also proposed to qualitatively assess the registration accuracy. It requires computing the transformations ${}^{CT}H_{CAD}$ and ${}^{CAD}H_{sc}$. As shown in Fig. 11, the lid model accurately fits the corresponding CT-scan images. The differences in the lower part of

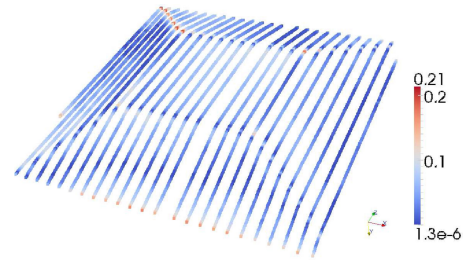


Fig. 9. Distribution of the distances in mm (blue to red) between the reconstructed SL points and the CT-scan planes.

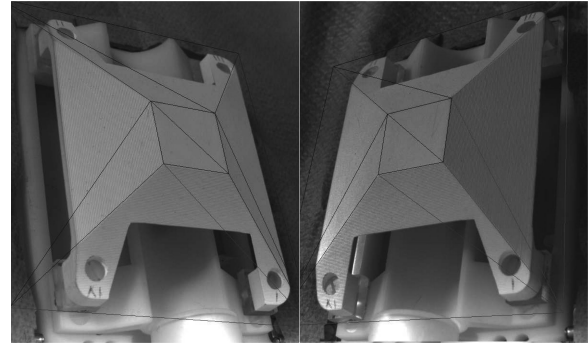


Fig. 10. Overlay in stereo camera views of the five planes of the lid, detected in $\{CT\}$, and registered in $\{sc\}$.

the lid can be explained by slight changes between the CAD model and the prototype.

In conclusion, though it is not easy to assess the registration accuracy in the absence of any gold standard, the two previous methods show significant results as they are based on geometric features that were not used for the registration computation (lid edges and hemispheric bed).

V. POSITIONING AND VISUAL SERVOING

A. Protocol

The knowledge of the needle geometry, together with the previous calibrations and registrations, allow computing the initial robot positioning to reach the planned target. However, the task achievement accuracy is affected by variabilities in the needle dimensions and in the mounting on the needle holder, and, more importantly, by the inaccuracy of the robot forward kinematic model. Visual servoing control was then proposed to refine the needle initial positioning, so as to reach submillimetric accuracy. Once the needle is properly positioned, it is retracted by the linear motor of the injector. The animal bed is then positioned in the robotic cell. Finally, the needle is inserted in the targeted organ. The accuracy of this back and forth motion is ensured by the micrometric repeatability of the linear motor, and by the synchronization of the insertion with respiratory cycles. The visual servoing procedure is fully automatic, based on the numerical derivation of the system model, known from the robot/camera calibration. It takes less than 1 min.

In the remainder of this section, we detail the first two steps of this protocol, the initial positioning and the visual servoing.

¹In a typical experiment, the RMS of the distances between the SL points and the associated planes was 0.019 ± 0.013 mm for a total of 8864 points, which shows the good quality of detection and 3-D reconstruction.

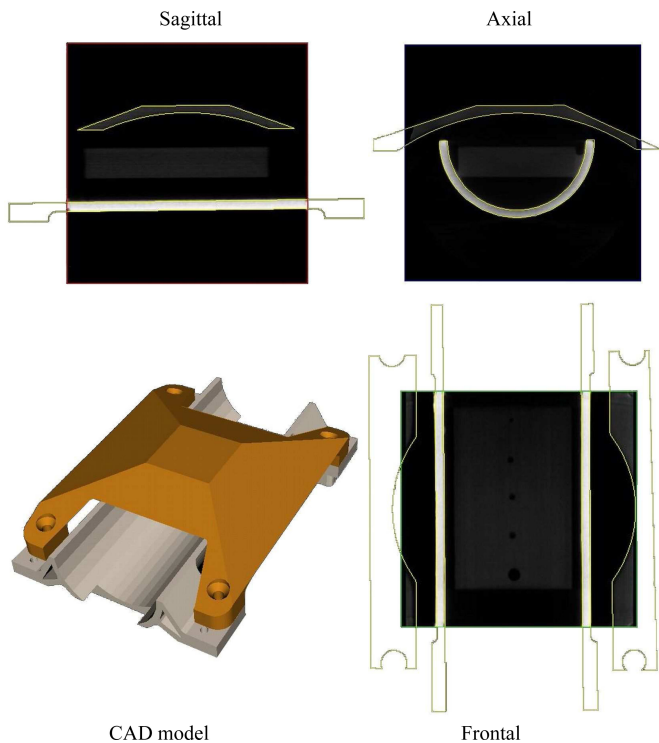


Fig. 11. Overlay of the lid model in the axial, sagittal, and frontal CT-scan images, after registration.

B. Initial Positioning

The positioning task consists in determining the robot joint coordinates q that correspond to the desired needle tip pose x . As the needle is symmetric along its main axis,² there is an infinite number of solutions for this problem, known as the inverse kinematics (IK). Then, the following iterative method is used to identify one of these configurations [23]. Let $x = (T_x, T_y, T_z, R_y, R_z)^T$ be the pose of the needle tip in $\{b\}$ and $q = (q_1, \dots, q_6)^T$ be the configuration of the robotic arm. The robot Jacobian matrix is $J(q) = \frac{\partial x}{\partial q}$. Its pseudoinverse J^+ can be used to find a numerical solution for the IK: one of the solutions can be obtained by iteratively adding the quantity

$$\Delta q = J^+ \Delta x \quad (3)$$

to the current joint coordinates, with Δx the difference between the desired needle tip pose and the one computed from the current joint coordinates, using the forward kinematics. A satisfactory solution is generally found after approximately 20 iterations. It serves as the starting robot configuration for the visual servoing process, thus limiting the initial error.

C. Visual Servoing

During the visual servoing phase, the needle holder is in the inserted position and without any animal in the robotic cell.

1) *Needle Detection*: The visual servoing task requires to measure the needle tip position and orientation in the stereo

²The used needles are short and their deformations are small, which explains that they are neglected in this study.

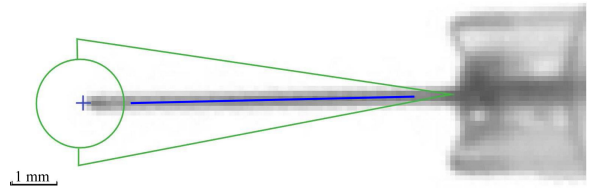


Fig. 12. Image of the needle with its ROI in green and the tip position and orientation detection in blue.

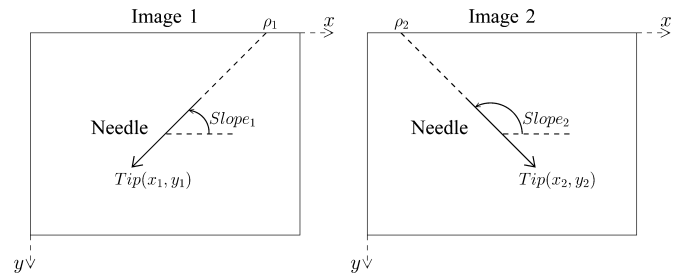


Fig. 13. Visual parameters associated with the needle in both cameras.

camera images. This is performed using classical image processing routines implemented in the opencv library [24]. A backlighting system integrated to the robotic cell is used to improve the needle detection.

At first, a circular region of interest (ROI) around the tip and an isosceles triangular ROI whose height is the needle axis are automatically defined by computing the reprojection of the theoretic position of the needle in each camera (see Fig. 12). Then, lines along the needle are detected in the triangular ROI using the Hough transform [25], in order to identify the needle borders. In order to limit illumination problems, the threshold accumulator parameter used in this method is changed until a significant number (typically 6–9) of long lines is obtained. Among these lines, the two most external ones are used to compute a central line that defines the needle axis. The needle tip is then computed as the intersection of the axis with its perpendicular, passing through the end of the bevel. This latter is determined using a Harris detector [26] in the circle ROI, with a subpixellic accuracy in each camera.

2) *Visual Parameters*: Both in the 3-D space and in the stereo camera images, the needle pose is characterized by five parameters. In an image, three parameters determine the needle tip position and its orientation. In the stereo camera system, six parameters are therefore associated to the needle tip, but only five are required. Actually, the tip position in the second image is subject to the epipolar constraint. Then, the tip position on the epipolar line is the only required parameter for the second image [19]. For practical reasons, the needle tip position and orientation are finally defined by the following five visual parameters: $x_1, y_1, Slope_1, Slope_2, \rho_2$ (see Fig. 13), with (x_1, y_1) the tip position in the first camera image, $Slope_i$ the angle between the needle axis and the i th camera image x -axis, and ρ_2 the abscissa of the intersection between the needle axis and the second camera image x -axis.

3) *Control*: Let $x_e = (t_x, t_y, t_z, r_x, r_y, r_z)$ and $v = (x_1, y_1, Slope_1, Slope_2, \rho_2)$, respectively, represent the robot end

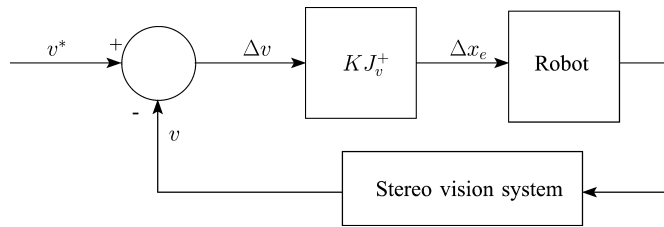


Fig. 14. Visual servoing block diagram.

effector pose and the visual parameters. Let $v = f(x_e)$ be the 5-D function relating these two vectors. The interaction matrix $J_v = \frac{\partial f}{\partial x_e}$ is the Jacobian of the f function [27]. It locally relates the motions of the visual parameters to those of the end effector. It is computed using the numerical differentiation of $v = f(x_e)$. To that end, the tip position and the direction of the needle are reprojected in both camera views by applying the transformation matrix ${}^c_i H_n = {}^c_i H_{sc} {}^{sc} H_b {}^b H_e {}^e H_n$, where the elementary transformations have been determined in Sections III-B2 and III-C.

With the knowledge of the interaction matrix, it is possible to implement a simple visual servoing scheme (see Fig. 14) to move the needle tip, so as to change the current measured visual parameters v into the desired ones v^* . Similarly to Section V-B, the pseudoinverse of J_v is used to compute Δx_e , the necessary relative motion of the end effector

$$\Delta x_e = K J_v^+ \Delta v \quad (4)$$

with $\Delta v = v^* - v$, and K a positive scalar used to tune the control convergence rate ($K = 0.7$ in our experiments). The resulting pose is then sent to the robot controller. Since successive poses are sent and not, as usual, Cartesian velocities, this visual servoing behaves like an iterative look-then-move loop. The robot moves toward the goal step by step, the size of the steps decreasing exponentially. At each step, after the measurement of the visual parameters, a new relative motion is computed, until Δv is below a given threshold in both images. This threshold is chosen around the detection noise value.

A perfect numerical model has been used to validate this procedure. After having placed the needle in a workspace of 50 mm^3 around the target, the visual servoing algorithm converged to the exact position in less than five iterations. In a real case, more than 10 iterations are necessary to reach the tolerance because of needle detection noise. The final result is very satisfactory, as visually illustrated in Fig. 15.

VI. SYSTEM ASSESSMENT AND *In Vivo* EXPERIMENTS

A. Preliminary Tests

Before investigating needle positioning accuracy *in vivo*, experiments were first performed *in vitro* for ethical reasons.

To assess the ability to insert the needle into a target identified in the CT images, a gelatin phantom has been molded in the animal bed. Air bubbles ranging from 2.0 to 14.9 mm^3 were inserted in the phantom to mimic tumors. Such a bubble appears as a hypodense area in μCT -scan images. The different targets were then defined as the bubble centers. After visual

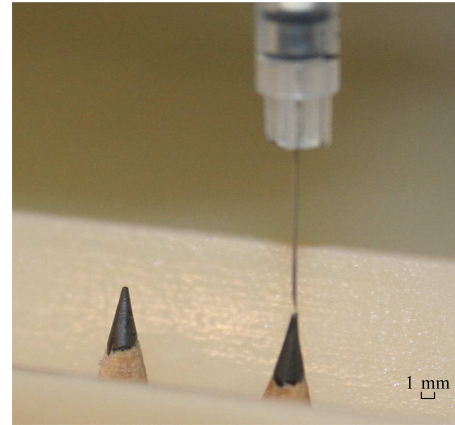
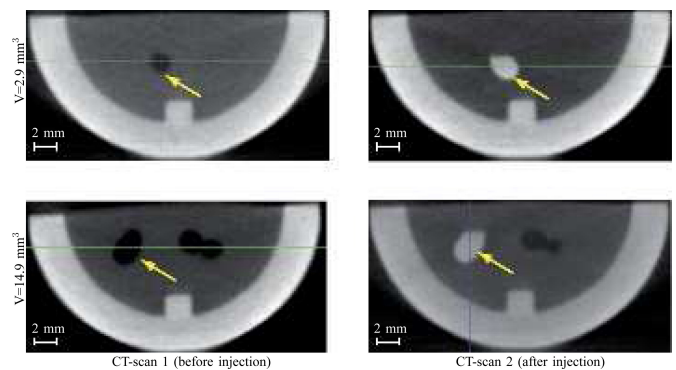


Fig. 15. Carbon tip as target.

Fig. 16. *In vitro* validation of needle insertion in gelatin phantom. Fenestra LC contrast agent is injected in air bubbles (yellow arrows) after robotic needle positioning at the center of the bubbles. Scale bar: 2 mm.

servoing and insertion according to the described procedure, a small amount of contrast agent was injected. In this preliminary test, accurate needle positioning was observed for 100% of the targets ($n = 10$), as demonstrated by the filling of the bubbles visible in the control images in Fig. 16.

B. Needle Positioning Accuracy Measurement in a Soft Wax

To quantitatively measure the needle positioning error, 60 different insertions were then planned and performed in a soft wax phantom. Tip coordinates and needle orientation were determined in the μCT -scan images from the needle trace in the wax. The error was then evaluated as the difference between planned and actual needle tip position. For this experiment, a wax/solvent mix (80:20) was preferred to gelatin to assess the positioning of the needle. With this wax, the needle path is better preserved after needle removal, whereas it tends to collapse in gelatin, thus inducing a bias in needle tip identification. Besides, the wax phantom was optimized in order to minimize needle deflection (less than voxel size), which is also important to assess the accuracy of the needle positioning. From these experiments, a 0.3 mm position error RMS was measured at the needle tip. However, the error is not isotropic: the mean error along X and Z was $0.17 \pm 0.091 \text{ mm}$ and $0.13 \pm 0.093 \text{ mm}$, respectively, whereas the mean error along the Y-axis (the needle axis) was

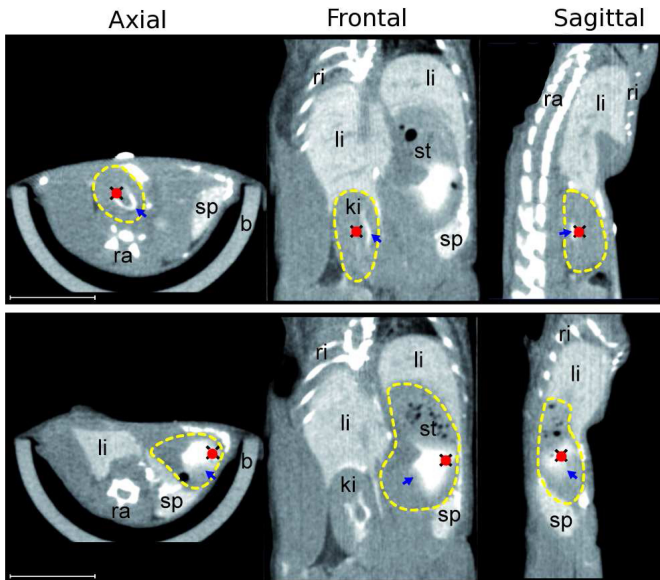


Fig. 17. *In vivo* validation of robotized needle insertion. Under anesthesia, the mouse was attached to the animal bed, using a sterile sticky surgical field. After μ CT-scan imaging, targets were defined inside the right kidney and the stomach. Using robotized automated needle insertion, $30 \mu\text{l}$ of a mixture of agarose and contrast agent were injected to create contrasted phantoms, and the position of these phantoms were verified on a second μ CT-scan, highlighting the targeted positions (black cross with red point) in the kidney or the stomach (delineated by a yellow-dotted line in the upper and lower panel, respectively). The phantom is evidenced by a black arrow—b: animal bed; ki: kidney; li: liver; ra: rachis; ri: ribs; sp: spleen; st: stomach. Scale bar: 10 mm.

0.38 ± 0.25 mm, due to partial volume effect as the 0.35 mm at the extremity of the needle bevel is below the resolution of the μ CT-scan image (see Fig. 4, dotted line in the close-up view of the needle). Thus, there is a systematic bias along this needle axis, and the calculated position error RMS is overestimated.

As typical visible tumors in the animal models are not smaller than 1 mm^3 , the *in vitro* results were satisfactory and justified the *in vivo* evaluation of the procedure.

C. In Vivo Needle Positioning Accuracy Measurement

The main constraints during *in vivo* experiments are internal organ displacements due to breathing and needle puncture. During the experiments, needle insertion was respiratory gated, as for μ CT-scan image acquisition, at the end of the expiratory phase. In addition, needles were inserted at high velocity (≈ 400 mm/s) so as to facilitate penetration and reduce organs motions [28]. As determining the needle position inside the animal was hardly technically feasible, a small amount of a mixture of gelling agarose and Telebrix iodinated contrast agent [29] was injected at the targeted positions. Mixing Telebrix with melted agarose at 50°C helped to reduce diffusion and clearance of contrast agent during the control scan, as it is quickly gelled at the animal body temperature. As shown in Fig. 17, contrast agent could be detected in the vicinity of the targeted position, demonstrating the robustness of the whole procedure.

All these experiments were supervised using an adequate HMI, partially illustrated in Fig. 18. Its main functionalities are:

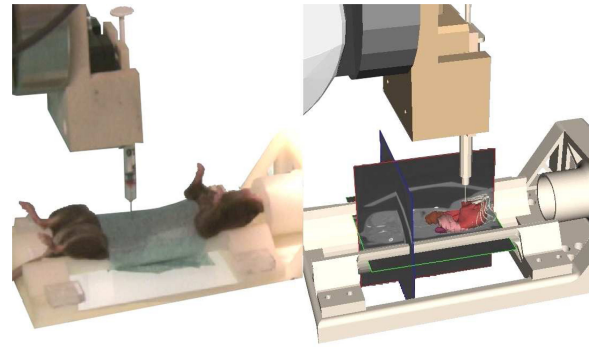


Fig. 18. Injection in an anesthetized mouse: real (left) and virtual view (right).

- 1) the definition the needle type, the identification of the mouse;
- 2) the pointing of some characteristic points (entry point, target, bed lid points);
- 3) the visualization of the scanner slices;
- 4) the visualization of the stereo images for calibration, SL, visual servoing;
- 5) the calibration procedures assistance.

VII. CONCLUSION

In this paper, we have presented the design of a system dedicated to image-guided punctures in small animals. Performing such minimally invasive procedures in small animals requires very accurate image guidance. As we showed in the present contribution, needle positioning accuracy is improved by the use of a robot, which assists the operator. While during last years, several needle insertion robots have been developed, most of them have not been tested *in vivo*. To our knowledge, only one system was efficiently used in these conditions, for the intratumoral measurement of pO_2 in subcutaneous tumors [1]. The main contribution of the present system is to offer a versatile system able to reach smaller targets in the animal and not only superficial ones.

The different steps of the system design, calibration, registration, and control have been presented throughout this paper. Methods were developed to assess and to improve, respectively, the robot/world and the CT-scan/cameras registrations. The robot/world registration was obtained by minimizing the reprojection error. The CT-scan/cameras registration was obtained by matching two sets of planes, measured, respectively, in the medical images and in a stereo camera system. Additionally, we proposed a method to calibrate independently intrinsic and extrinsic parameters of the stereo camera system. Finally, the ability of the prototype to fulfill the accuracy requirements was validated both *in vitro* and *in vivo*. It essentially relies on the refinement of the needle tip placement, using a stereo visual servoing.

Future applications will include the evaluation of new therapeutics injected intratumorally in tumor animal models. Preliminary results showed that the administration of a common antimetabolic agent intratumorally using the robot is superior to manual intraperitoneal injection on a mouse liver tumor model.

Another challenge will consist in the development of a biopsy device, to retrieve biological samples from target organs or tumors. This will be very useful for the biological research, in order to follow the evolution of a tumor in the same animal by recurrent biopsies without opening or killing the animal.

ACKNOWLEDGMENT

The authors wish to thank Dr. A. Ayadi for his previous work and Dr. L. Soler and Prof. J. Marescaux, from IRCAD, for their continuous support. This work is dedicated to the memory of their colleague and friend P. Graebing, who brought his legendary enthusiasm and his deep knowledge of computer vision to this project.

REFERENCES

- [1] J. Chang, B. Wen, P. Kazanzides, P. Zanzonico, R. D. Finn, G. Fichtinger, and C. C. Ling, "A robotic system for f-fmiso pet-guided intratumoral pO₂ measurements," *Med. Phys.*, vol. 36, pp. 5301–5309, 2009.
- [2] P. Kazanzides, J. Chang, I. Iordachita, J. Li, C. C. Ling, and G. Fichtinger, "Development of an image-guided robot for small animal research," *Comput. Aided Surg.*, vol. 12, pp. 357–365, 2007.
- [3] Y. Huang, T. Wu, M. Lin, C. Yang, W. Guo, Z. Wang, C. Chen, and J. Lee, "An automated robot arm system for small animal tissue biopsy under dual-image modality," *Nuclear Instrum. Methods Phys. Res.*, vol. 569, pp. 230–234, 2006.
- [4] A. Waspe, H. Cakiroglu, J. Lacefield, and A. Fenster, "Design and validation of a robotic needle positioning system for small animal imaging applications," in *Proc. IEEE Biomed. Eng. Soc. Conf.*, Aug./Sep. 2006, pp. 412–415.
- [5] A. Waspe, J. Lacefield, and A. Fenster, "Registration of three-dimensional high-frequency ultrasound images to a robotic needle-positioning system for pre-clinical research," in *Proc. IEEE Int. Symp. Biomed. Imag. Nano Macro*, Apr. 2007, pp. 1132–1135.
- [6] A. Waspe, D. McErlain, V. Pitelka, D. Holdsworth, J. Lacefield, and A. Fenster, "Integration and evaluation of a needle-positioning robot with volumetric micro-computed tomography image guidance for small animal stereotactic interventions," *Med. Phys.*, vol. 37, no. 4, pp. 1647–1659, 2010.
- [7] O. Bebek, M. Hwang, B. Fei, and M. Cavusoglu, "Design of a small animal biopsy robot," in *Proc. IEEE Biomed. Eng. Soc. Conf.*, Aug. 2008, pp. 5601–5604.
- [8] M. Hwang, O. Bebek, B. Fei, and M. C. Cavusoglu, "Kinematic calibration of a parallel robot for small animal biopsies," in *Proc. IEEE/RSJ Int. Conf. Intell. Robot. Syst.*, Oct. 2009, pp. 4104–4109.
- [9] O. Bebek, M. J. Hwang, and M. C. Cavusoglu, "Design of a parallel robot for needle-based interventions on small animals," *IEEE/ASME Trans. Mechatron.*, vol. 18, no. 1, pp. 62–73, Feb. 2013.
- [10] L. Ramrath, U. G. Hofmann, and A. Schweikard, "A robotic assistant for stereotactic neurosurgery on small animals," *Int. J. Med. Robot. Comput. Assist. Surg.*, vol. 4, no. 4, pp. 295–303, 2008.
- [11] A. Waspe, H. Cakiroglu, J. Lacefield, and A. Fenster, "Design, calibration and evaluation of a robotic needle-positioning system for small animal imaging applications," *Phys. Med. Biol.*, vol. 52, no. 7, pp. 1863–1878, 2007.
- [12] A. Ayadi, B. Bayle, P. Graebing, and J. Gangloff, "An image-guided robot for needle insertion in small animal. Accurate needle positioning using visual servoing," in *Proc. IEEE/RSJ Int. Conf. Intell. Robot. Syst.*, Nice, France, Sep. 2008, pp. 1453–1458.
- [13] A. Ayadi, G. Bour, P. Aprahamian, B. Bayle, P. Graebing, J. Gangloff, L. Soler, J.-M. Egly, and J. Marescaux, "Fully automated image-guided needle insertion: Application to small animal biopsies," in *Proc. IEEE Biomed. Eng. Soc. Conf.*, Lyon, France, Aug. 2007, pp. 194–197.
- [14] Z. Zhang, "A flexible new technique for camera calibration," *IEEE Trans. Pattern Anal. Mach. Intell.*, vol. 22, no. 11, pp. 1330–1334, Nov. 2000.
- [15] Y. Shiu and S. Ahmad, "Finding the mounting position of a sensor by solving a homogeneous transform equation of the form $ax = xb$," in *Proc. IEEE Int. Conf. Robot. Autom.*, Mar. 1987, vol. 4, pp. 1666–1671.
- [16] R. Y. Tsai and R. K. Lenz, "A new technique for fully autonomous and efficient 3-D robotics hand/eye calibration," *J. Robot. Autom.*, vol. 5, pp. 345–358, 1989.
- [17] F. Dornaika and R. Horaud, "Simultaneous robot-world and hand-eye calibration," *Trans. Robot. Autom.*, vol. 14, pp. 617–622, 1998.
- [18] P. Graebing, C. Boucher, C. Daul, and E. Hirsch, "3D sculptured surface analysis using a structured-light approach," *Proc. SPIE Object Environ. Model.*, vol. 2598, pp. 128–139, 1995.
- [19] O. Faugeras, *Three-Dimensional Computer Vision: A Geometric Viewpoint*. Cambridge, MA, USA: MIT Press, 1993.
- [20] P. J. Besl and H. McKay, "A method for registration of 3-D shapes," *IEEE Trans. Pattern Anal. Mach. Intell.*, vol. 14, no. 2, pp. 239–256, Feb. 1992.
- [21] K. Arun, T. Huang, and S. Blostein, "Least-squares fitting of two 3-D point sets," *IEEE Trans. Pattern Anal. Mach. Intell.*, vol. PAMI-9, no. 5, pp. 698–700, Sep. 1987.
- [22] J. M. Fitzpatrick, "Fiducial registration error and target registration error are uncorrelated," *Proc. SPIE Med. Imag.*, vol. 7261, pp. 726102-1–726102-12, 2009.
- [23] S. Chiaverini, G. Oriolo, I. Walker, "Kinematically Redundant, Manipulators," in *Handbook of Robotics.*, New York, NY, USA: Springer-Verlag, 2008.
- [24] G. Bradski and V. Pisarevsky. (2012). Opencv [Online]. Available: <http://www.willowgarage.com/pages/software/opencv>
- [25] N. Kiryati, Y. Eldar, and A. Bruckstein, "A probabilistic hough transform," *Pattern Recog.*, vol. 24, no. 4, pp. 303–316, 1991.
- [26] C. Harris and M. Stephens, "A combined corner and edge detection," in *Proc. 4th Alvey Vis. Conf.*, 1988, pp. 147–151.
- [27] B. Espiau, F. Chaumette, and P. Rives, "A new approach to visual servoing in robotics," *IEEE Trans. Robot. Autom.*, vol. 8, no. 3, pp. 313–326, Jun. 1992.
- [28] B. Maurin, L. Barbé, B. Bayle, P. Zanne, J. Gangloff, M. de Mathelin, L. Soler, and A. Forgione, "In vivo study of forces during needle insertions," presented at the Med. Robot. Navigat. Vis. Sci. Workshop, Remagen, Germany, 2004.
- [29] A. Rethy, T. Lango, J. Aasland, and R. Marvik, "Development of a multimodal tumor model for porcine liver," *J. Gastrointest. Surg.*, vol. 14, pp. 1969–1973, 2010.



Laurent Goffin received the M.S. degree in medical computer science from the University Pierre et Marie Curie, Paris, France, in 2000.

From 2000 to 2001, he was a Design Engineer at the ChIR team at the Institut National de Recherche en Informatique et en Automatique, Sophia Antipolis, France. He then worked for five years on biomedical software programming in the VirtualS team at the Institut de Recherche contre le Cancer de l'Appareil Digestif, Strasbourg, France. Since 2010, he has been working with the Control, Vision and Robotics Team at ICube Laboratory University of Strasbourg, Strasbourg, France. His research interests include augmented reality, computer vision and robotics.



Gaétan Bour received the Engineering and M.S. degrees in biotechnology from the Ecole Supérieure de Biotechnologie de Strasbourg, Strasbourg, France, in 2002, and the Ph.D. degree in molecular and cellular biology from the University Louis Pasteur, Strasbourg, in 2006.

Since 2007, he has been a Research Scientist at the Laboratoire de Biologie des Tumeurs, Institut de Recherche contre le Cancer de l'Appareil Digestif, Strasbourg. His current research interests include translational approaches for *in vitro* and *in vivo* cancer modeling and analysis.



Fernand Martel received the M.S. degree in engineering and technology with a specialty in industrial computing and automated systems from the University of Strasbourg, Strasbourg, France, in 2008.

During the period 2008–2012, he was a Design Engineer with the IGBMC Laboratory, Illkirch-Graffenstaden, France. In 2012, he became a Biomedical Engineer at the IHU-Strasbourg, Strasbourg, France. His research interest includes prototype design and automated systems.



Jean-Marc Egly received the Ph.D. degrees in chemistry and biochemistry from Louis Pasteur University, Strasbourg, France, in 1970 and 1976, respectively.

He gained expertise in molecular biology. Since 1985, he has been the Directeur de Recherche at Inserm and lead a group at the Institut de Recherche contre les Cancers de l'Appareil Digestif, Strasbourg, and Institut de Génétique et de Biologie Moléculaire et Cellulaire. His research interest aims to understand the mechanism that regulates gene expression and the maintenance of genome integrity. His work has

provided molecular explanations for many clinical features of several human diseases including rare disorders and cancer.

Dr. Egly has been a member of the Académie des Sciences since 2005.



Stéphane Nicolau was born on 25th January 1978. He received the Engineer Diploma from the Ecole Nationale Supérieure de Physique de Strasbourg (now Télécom Physique Strasbourg), Strasbourg, France, in 2000. He received the Ph.D. degree from the INRIA Sophia-Antipolis, Sophia Antipolis, France, in 2004, under the supervision of Nicholas Ayache, Head of the ASCLEPIOS team (former EPIDAURE).

He joined the Virtual Reality team of the Institut de Recherche contre les Cancers de l'Appareil Digestif (IRCAD), Strasbourg, as a Researcher. In 2009, he

became in IRCAD TAIWAN the Leader of the new research team in medical imaging and launched several projects related to computer-assisted system for orthopaedic surgery, endoscopic image undistortion and ultrasound simulator. He came back to IRCAD France in 2011 and currently supervises the research team. His main fields of interest include medical augmented reality, medical image processing, 3-D modelling of anatomical deformations, calibration of vision systems, and validation of medical guidance systems.



Bernard Bayle received the agrégation in electrical engineering from Ecole Normale Supérieure de Cachan, Cachan, France, in 1995. He received the M.S. and Ph.D. degrees in control theory and robotics from the University of Toulouse (LAAS-CNRS), Toulouse, France, in 1996 and 2001, respectively.

He became Maître de Conférences at the Ecole Nationale Supérieure de Physique de Strasbourg (ENSPS), Strasbourg University, Strasbourg, France, in 2002, where he has created the ICT and healthcare curriculum. He has been a Professor at ENSPS, now

Télécom Physique Strasbourg, since 2011. He is currently a member of the Control, Vision and Robotics research group of the ICube Laboratory, University of Strasbourg. He is Coordinator of the medical robotics theme at CNRS robotics research group. His research interests include design, modeling, and control of robotic systems, with a focus on medical robotics and force feedback technologies.



Jacques Gangloff graduated from the Ecole Normale Supérieure de Cachan, Cachan, France, in 1995. He received the M.S. and Ph.D. degrees in robotics from the University Louis Pasteur, Strasbourg, France, in 1996 and 1999, respectively.

Between 1999 and 2005, he was an Associate Professor with the University of Strasbourg. In 2005, he was a Nominated Professor at the same University. He is currently member of the AVR (Control Vision and Robotics) team at the ICube Laboratory, University of Strasbourg, Strasbourg. His research interests

include mainly visual servoing, predictive control, medical robotics and more recently cable driven parallel robotics.

Dr. Gangloff received the Best Vision Paper Award at the IEEE International Conference on Robotics and Automation (ICRA 2004), the 2005 Best Paper Award of the IEEE TRANSACTIONS ON ROBOTICS AND AUTOMATION and the Best Conference Paper Award at the IEEE/RAS-EMBS International Conference on Biomedical Robotics and Biomechatronics (BIOROB 2010).